Electron acceleration at oblique angles via stimulated Raman scattering at laser irradiance $>10^{16}$ W cm^{-2} μm^2

A. Higginson,[1] S. Zhang,[1] M. Bailly-Grandvaux,[1] C. McGuffey,[1] K. Bhutwala,[1] B. J. Winjum,[2] J. Strehlow,[1] B. Edghill,[1] M. Dozières,[1] F. S. Tsung,[3] R. Lee,[3] S. Andrews,[4] S. J. Spencer,[5] N. Lemos,[4] F. Albert,[4] P. King,[6,4] M. S. Wei,[7] W. B. Mori,[3] M. J.-E Manuel,[8] and F. N. Beg[1,*]

[1]*Center for Energy Research, University of California San Diego, 9500 Gilman Drive, La Jolla, California 92093-0417, USA*
[2]*Office of Advanced Research Computing, University of California Los Angeles, Los Angeles, California 90095, USA*
[3]*Physics and Astronomy Department, University of California Los Angeles, Los Angeles, California 90095, USA*
[4]*Lawrence Livermore National Laboratory, Livermore, California 94550, USA*
[5]*Centre for Fusion, Space, and Astrophysics, University of Warwick, Coventry CV4 7AL, United Kingdom*
[6]*Department of Physics, University of Texas at Austin, Austin, Texas 78712, USA*
[7]*Laboratory for Laser Energetics, University of Rochester, Rochester, New York 14623-1299, USA*
[8]*General Atomics, Inertial Fusion Technologies, San Diego, California 92121, USA*

(Received 31 July 2020; revised 28 November 2020; accepted 22 January 2021; published 18 March 2021)

The generation of hot, directional electrons via laser-driven stimulated Raman scattering (SRS) is a topic of great importance in inertial confinement fusion (ICF) schemes. Little recent research has been dedicated to this process at high laser intensity, in which back, side, and forward scatter simultaneously occur in high energy density plasmas, of relevance to, for example, shock ignition ICF. We present an experimental and particle-in-cell (PIC) investigation of hot electron production from SRS in the forward and near-forward directions from a single speckle laser of wavelength $\lambda_0 = 1.053\,\mu$m, peak laser intensities in the range $I_0 = 0.2$–1.0×10^{17} Wcm^{-2} and target electron densities between $n_e = 0.3$–$1.6\%\ n_c$, where n_c is the plasma critical density. As the intensity and density are increased, the hot electron spectrum changes from a sharp cutoff to an extended spectrum with a slope temperature $T = 34 \pm 1$ keV and maximum measured energy of 350 keV experimentally. Multidimensional PIC simulations indicate that the high energy electrons are primarily generated from SRS-driven electron plasma wave phase fronts with k vectors angled $\sim50^\circ$ with respect to the laser axis. These results are consistent with analytical arguments that the spatial gain is maximized at an angle which balances the tendency for the growth rate to be larger for larger scattered light wave angles until the kinetic damping of the plasma wave becomes important. The efficiency of generated high energy electrons drops significantly with a reduction in either laser intensity or target electron density, which is a result of the rapid drop in growth rate of Raman scattering at angles in the forward direction.

DOI: 10.1103/PhysRevE.103.033203

I. INTRODUCTION

The propagation and energy coupling of intense laser pulses in plasma is fundamental to laser-driven inertial confinement fusion (ICF) [1] and can play an important role in any laser-plasma-based experiments and simulations that feature an underdense plasma. As the laser propagates in an underdense plasma, a number of laser plasma instabilities (LPIs) [2,3] may occur and grow under appropriate conditions, significantly interfering with the laser beam's propagation dynamics [4,5] and coupling processes. They can manifest and result in filamentation of the laser beam [6], energy transfer between multiple beams co-propagating in a plasma [7], hot electron generation [8], and energy loss through parametric decay instabilities that reflect the incident light. Collectively, they are one of the biggest issues impeding the success of ICF programs.

One parametric decay instability that has received considerable attention over the past half century is stimulated Raman scattering (SRS) [4,5,9], which is the resonant decay of the incident light wave into a scattered light wave and an electron plasma wave (EPW). The study of SRS has been motivated mainly due to its deleterious role in ICF schemes, accounting for the largest single fraction of energy loss on current ignition-scale experiments [10,11], in addition to its close connection to plasma-based acceleration [12,13]. Additionally, the damping of high phase velocity EPWs can result in the generation of superthermal electrons, typically producing over 50 kJ of hot electrons on ignition-scale experiments [14]. These electrons have a significant impact on the dynamics of both direct- and indirect-drive ICF schemes and can, for example, result in preheating of the imploding fuel due to electron energy deposition in the fuel material. Implosion symmetry can also be affected, of high importance in achieving maximum gain.

The evolution of SRS, which is dependent on the laser and plasma parameters, and accelerated electrons has been

*fbeg@eng.ucsd.edu

well documented for parameter regimes relevant to current ICF conditions. These experiments typically operate using a laser intensity $I_0 \sim 10^{15}$ Wcm^{-2} (corresponding to an irradiance $I\lambda^2 \sim 10^{14}$ Wcm$^{-2}\mu$m^2) [3,15,16]. The number of experiments of a single laser speckle performed using $I\lambda^2 = 10^{15-17}$ Wcm$^{-2}\mu$m^2 (normalized laser amplitude of up to $a_0 \sim 0.2$) and at keV temperatures is relatively small, highlighted in a recent review article by Craxton *et al.* [2]. These laser irradiances were in fact used during the first experimental demonstrations of forward SRS [17,18]. Such irradiances are now relevant to shock ignition (SI) ICF [19], which involves the generation of a strong shock after compression using a $I_0 \sim 10^{16}$ Wcm^{-2} laser pulse to ignite the central hot spot. For SI, the presence of LPI-driven hot electrons can affect the interaction dynamics drastically [20–23]. They possess a high energy relative to the ambient electron temperature and can propagate beyond the ablation zone and deposit their energy near the shock front. This can be both advantageous or deleterious for SI, depending on their stopping range in the compressed capsule [20,21]. In advantageous scenarios, the effect of hot electrons has been measured to increase the shock ablation pressure by 30% [22,23], with hot electron measurements in the context of SI for $I\lambda^2 \sim 10^{15}$ Wcm$^{-2}\mu$m^2 being recently reported [22–24]. Simulations for high intensity pulses and relatively cold, moderate density plasmas have also been reported [25].

In this article, we investigate SRS-driven electron acceleration via experimental and numerical methods using peak laser intensities in the range $I_0 = 0.2$–1.0×10^{17} Wcm^{-2} and laser wavelength $\lambda_0 = 1.053\mu$m. We focus our study on hot (electron temperature $T_e \sim 1.5$ keV), underdense helium plasmas with electron densities $n_e = 0.3$–1.6% n_c (where n_c is the plasma critical density, at which the plasma frequency ω_p equals the laser frequency ω_0). Through particle-in-cell (PIC) simulations and analytical arguments [26], we attribute the strong presence of superthermal electrons measured in our parameter space to be the result of electron acceleration in plasma waves associated with near-forward SRS. For our parameter space, near-forward SRS has a spatial growth rate optimized at relatively large oblique angles with respect to the laser pulse, concurrent with the analytical framework outlined in Wilks *et al.* [26]. We note that similar observations were made in the mid-1980s by Forslund *et al.* [27] and Mori *et al.* [28] where they observed SRS generated plasma waves to also be congregated at an angle oblique to the laser propagation direction (at an angle near $\sim50^\circ$). Similar dynamics have also been noted again recently in the context of SRS driven during cross-beam energy transfer [29]. Using the theory in Ref. [26] and geometrical arguments in Refs. [27,28] we show that, for the parameters in this earlier simulation work and in this paper, the spatial growth of SRS is largest when the scattered light propagates at angles in the forward direction and the EPWs propagate obliquely.

The paper is structured as follows: In Sec. II, we discuss the experiment diagnosing the fast electrons which we attribute to SRS forward scatter at oblique angles and present the measured electron spectra. In Sec. III, numerical simulation results are shown and compared with the experimental results to investigate the underpinning physics involved in the generation of the diagnosed hot electrons, where we identify EPWs propagating at oblique angles with respect to the laser k vector. Finally, in Sec. IV, we discuss the spatial growth rate of SRS-driven plasma waves as a function of scattering angle and investigate how this changes as a function of laser intensity and plasma electron density.

II. EXPERIMENTAL SETUP AND MEASUREMENTS OF ACCELERATED ELECTRONS

The experiment was performed at the Titan laser facility, Lawrence Livermore National Laboratory (LLNL). Titan's short pulse beam was used, operating with $\lambda_0 = 1.053\,\mu$m, temporal duration $\tau_0 = 200$ ps [full width at half maximum (FWHM)] and variable total energy on-target in the range $E_0 = 50$–170 J. The beam is stretched by changing the effective spacing of the gratings in the compressor, which resulted in a slight frequency chirp of the laser as a function of time. This was measured with a spectrometer coupled to a streak camera, and amounted to a $\sim$5-nm change as a function of time (higher wavelength at earlier times). This has a negligible effect on the LPI dynamics under investigation here. The beam was focused using an $f/10$ off-axis parabolic mirror (OAP) to an elliptical spot of diameter $d_0 = 16 \times 27$ μm^2 (FWHM), as determined from focal spot images. By using an OAP (i.e., reflective-based focusing optic), we ensure that light of all wavelengths constituting the 5-nm bandwidth laser pulse focus to the same point in space. Centered on the maximum, a circle of diameter $d_0 = 30\,\mu$m contains $0.25E_0$. The beam is Gaussian in both time and space, with the aforementioned parameters resulting in an average intensity range $I_{\text{ave}} = 1$–3×10^{16} Wcm^{-2}. To facilitate comparison to the PIC simulations shown in the following section, which simulate only the high intensity part of the pulse temporally and spatially, we instead refer to the laser intensity in terms of the peak (in time and space) intensity value. This corresponds to a range $I_0 = 2$–6×10^{16} Wcm^{-2} experimentally. The beam was focused in the center of a helium (He) gas, generated by a supersonic gas jet nozzle with aperture diameter equal to 4 mm and design Mach number $M = 6.3$. Irradiation of the He gas by the leading edge of the laser pulse results in the creation of a quasihomogeneous plasma, as determined by radiation-hydrodynamic simulations detailed in the following section. As the main pulse arrives, SRS is seeded and EPWs are driven. The damping of these waves results in the acceleration of hot electrons [13]. The accelerated electrons were sub-sampled using an electron, proton, positron spectrometer (EPPS) [30] containing BAS-SR image plate as the detecting media [31], situated 63 cm downstream of the interaction region and angled 7° below the horizontal laser propagation axis. The electron spectrometer collects electrons in a solid angle equal to 4.7×10^{-5} Sr. A schematic of the experimental setup is shown in Fig. 1(a).

The plasma electron density was varied by adjusting the backing pressure of the gas jet system in the range $P = 200$–1000 psi, corresponding to a measured electron density $n_e = 0.3$–1.5% n_c. The electron density is determined via Abel inversion of interferograms recorded on each laser shot, using a coherent short pulse laser with $\lambda_0 = 0.527\,\mu$m and $\tau_0 = 70$ ps to probe the plasma transversely, $t = 700$ ps after arrival of

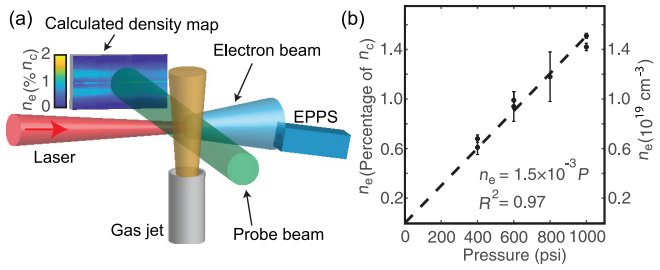

FIG. 1. (a) Schematic displaying the experimental configuration, where EPPS is the electron spectrometer. An example density map measured by the interferometer is shown, for a peak laser intensity $I_0 = 2 \times 10^{16}$ Wcm^{-2} and pressure $P = 400$ psi. The electron density (n_e) is shown as a percentage of the critical density (n_c). (b) Measured n_e as a function of P obtained from multiple interferograms for $I_0 = 2 \times 10^{16}$ Wcm^{-2}. The dashed black line is a linear fit to the data intercepting at $n_e = 0$, with the fit parameters labeled.

the peak of the main pulse. Abel inversion is performed using the wavelet analysis software NEUTRINO [32]. An example density map for $P = 400$ psi and $I_0 = 2 \times 10^{16}$ Wcm^{-2} is shown in Fig. 1(a). Figure 1(b) displays the calculated average (across the longitudinal direction) electron density extracted from multiple interferograms using several gas jet pressures for $I_0 = 2 \times 10^{16}$ Wcm^{-2}, exhibiting a clear linear trend. The error associated with the density measurement at the laser focal point is 6%, equal to the standard deviation of the fit to the data. Across the longitudinal axis, the variation in density is below 10% within a 1-mm distance from the focal point. Further details of the analytical technique for extracting electron density, associated errors, and additional example data images are given in Section A of the Supplemental Material [33]. Section B of the Supplemental Material contains simulation results and discussion that provide confidence in the quoted density measurements shown in Fig. 1(b) being reflective of the density during the interaction around $t = 0$ ps.

Figures 2(a)–2(c) display example electron spectra recorded by the electron spectrometer for $I_0 = (6, 4, 2) \times 10^{16}$ Wcm^{-2}, respectively, with consistent color schemes representing different values of n_e across the three subfigures.

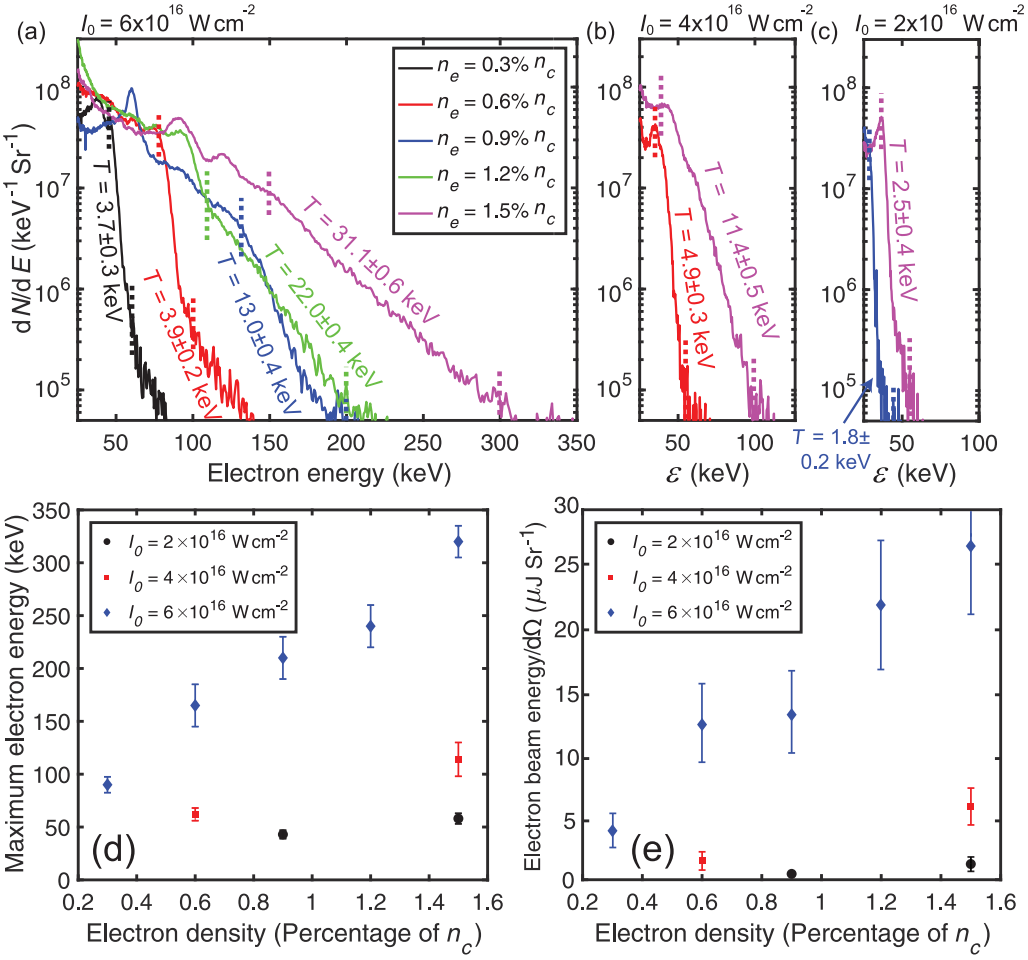

FIG. 2. (a)–(c) Electron spectra recorded by the electron spectrometer for five values of plasma electron density (n_e) and peak laser intensities (I_0) equal to (a) $I_0 = 6 \times 10^{16}$ Wcm^{-2}, (b) $I_0 = 4 \times 10^{16}$ Wcm^{-2}, and (c) $I_0 = 2 \times 10^{16}$ Wcm^{-2}. A temperature fit to each spectrum was performed, with the hot electron slope temperature (T) labeled next to the corresponding spectrum. The fit was performed in the range bound by the colored dashed vertical lines, where the electron temperature can be accurately described by a single temperature dependence. Note that the data series shown in (a)–(c) corresponds to the legend shown in (a). (d) Maximum electron energy ($\varepsilon_{\max}$) and (e) total energy contained in the accelerated electron population per solid angle (Ω) as a function of n_e for the three values of I_0 explored experimentally.

The hot electron slope temperatures (T) are labeled for the high energy portion of the corresponding spectra. Figure 2(d) displays the maximum energy of electrons detected ($\varepsilon_{\max}$) of the measured electrons shown in Figs. 2(a)–2(c) as a function of n_e, while Fig. 2(e) displays the total energy of the measured electrons. The error bars in Fig. 2(d) are a result of the uncertainty in distinguishing the electron signal above the noise level, while in Fig. 2(e) the error bars are a result of the uncertainty in converting from photostimulated luminescence to electron number—detailed in Bonnet *et al.* [31].

From the experimental data and analysis shown in Fig. 2, clear increases in the overall number of electrons, T and $\varepsilon_{\max}$ are measured as functions of both n_e and I_0. The clear parametric difference is that for the highest intensity and above a density threshold ($I_0 = 6 \times 10^{16}$ Wcm^{-2} and $n_e \geqslant 0.9\%\ n_c$) a two-temperature distribution is evident. This is indicative of two sets of distinct EPWs with different parameters: one responsible for generating the high energy tail of the electron distribution and the other generating the numerous, low energy electrons. The range that the temperature fits were performed within correspond to the regions where a single distribution is apparent. In the following section, representative simulation results are shown to explore the EPW dynamics and the generated spectra compared with the experimental results.

III. SIMULATIONS OF ELECTRON ACCELERATION DRIVEN BY NEAR-FORWARD STIMULATED RAMAN SCATTERING

To investigate the underlying physics responsible for the clear parametric dependencies of the accelerated electrons in our experiment, we incorporate a simulation workflow that uses two simulation codes. The first code used in this process is the radiation-hydrodynamic code FLASH [34], which is used to calculate T_e based on the laser and target parameters used experimentally, in addition to bench-marking the interferometry measurements as detailed in Section B of the Supplemental Material [33]. FLASH operates in two-dimensional (2D) cylindrical $R-z$ geometry and uses adaptive mesh refinement with a minimum grid size of 2 μm. The laser was injected along the z axis with $\tau_0 = 200$ ps (FWHM), irradiating a homogeneous He gas sphere of 4 mm diameter, with the target's atomic evolution calculated from PROPACEOS EOS and 6-group opacity tables. Within the temporal FWHM of the laser pulse, the calculated electron temperature is $T_e \sim 2$ keV at the center of the plasma and $T_e > 1$ keV within a cylindrical region of area 2 mm $\times$ 20 μm (longitudinal length and transverse radius, respectively). Note that the ionization state (Z) of the plasma at the leading edge of the main pulse is exclusively $Z = 2$ (i.e., fully ionized). Further, the plasma density over τ_0 is roughly constant, as shown in Section B of the Supplemental Material [33].

The second code used is the multidimensional PIC electromagnetic code OSIRIS 4.0 [35–37], which captures the LPI dynamics. We use 2D simulations in Cartesian geometry. The plasma was initialized as fully ionized, with a fixed electron temperature $T_e = 1.5$ keV (based on information obtained from the FLASH simulation discussed above) and electron densities of $n_e = 0.5\%\ n_c$, $1.0\%\ n_c$, and $1.6\%\ n_c$. The simulations use normalized parameters as each simulation corresponds to a family of cases with different absolute values for the laser wavelength and plasma density. Here we assume that the laser wavelength $\lambda_0 = 1.053\ \mu$m, for which the simulation box is 420 μm $\times$ 50 μm (longitudinal and transverse, respectively), with a 50-nm mesh resolution so as to resolve the Debye length ($\lambda_d \sim 90$ nm) and with 64 electrons and He ions per cell. The laser enters from the left vertical boundary and leaves from the right, and open boundary conditions are used for the fields and thermal bath boundary conditions for the particles at all four boundaries. The laser pulse has a flat-top duration $\tau_0 = 5$ ps (50-fs rise time) and spot size $d_0 = 6\ \mu$m (FWHM), corresponding to a beam waist radius $w_0 = 5\ \mu$m, which is roughly equal to half the FWHM spot size of the smallest dimension of the elliptical laser spot used experimentally. A smaller spot size was used to make the simulation more computationally tractable while retaining the essential physics. The simulation progresses in 0.06 fs time steps. The peak laser intensity investigated using the PIC simulations is in the range $I_0 = (0.3\text{–}1)\times 10^{17}$ Wcm^{-2}, simulating the highest intensity portion of the beam expected experimentally for each intensity case, as explained in the latter half of Section A in the Supplemental Material [33]. That discussion details the role of ponderomotive self-focusing [6,38], which is indicated in the interferometry data. By choosing to simulate the temporal and spatial pulse peak, we can elucidate the dynamics occurring at the highest intensity portion of the interaction.

To provide an overview of the overall behavior captured in the simulations representative of the laser-plasma interaction occurring in the high intensity region of the pulse experimentally, Figs. 3(a)–3(c) display the longitudinal electric field (E_x) of the EPWs at time $t = 4.3$ ps (where $t = 0$ ps refers to the laser leading edge entering the simulation domain at the left boundary) for three values of n_e, increasing from top to bottom, and $I_0 = 1 \times 10^{17}$ Wcm^{-2}. The red circles represent electrons with energy $\varepsilon > 150$ keV. The electron spectra over the entire displayed region of the simulation box at $t = 4.3$ ps are shown in Fig. 3(d) for the three density cases. With comparison to the experimental spectra shown in Fig. 2(a), the spectra are similar in terms of overall trend and $\varepsilon_{\max}$, providing confidence that the simulations are reflective of the physics occurring in the experiment at the peak intensity. In particular, a two-temperature distribution is apparent for the $n_e \geqslant 1.0\%\ n_c$ cases, with a sharp fall-off present in the low density case. The low intensity simulations do not exhibit a two-temperature distribution, and we therefore focus our discussion to explaining the density dependence for the high intensity cases.

For all three density cases simulated, SRS forward scatter is observed, as evidenced by the nonzero E_x regions indicative of EPWs in the center of the simulation box in Figs. 3(a)–3(c), with a wave vector parallel to the laser propagation axis. Unique to the two higher density simulations is the generation of near-forward SRS close to the right boundary of the simulation domain displayed, which results in generated EPWs with plasma wave angles $\theta = 45^\circ$–60° with respect to the laser axis. This near-forward SRS first grows obliquely near the focal spot of the laser and subsequently evolves convectively in the forward direction, with the EPWs reaching largest amplitude near the end of the simulation domain. Additional

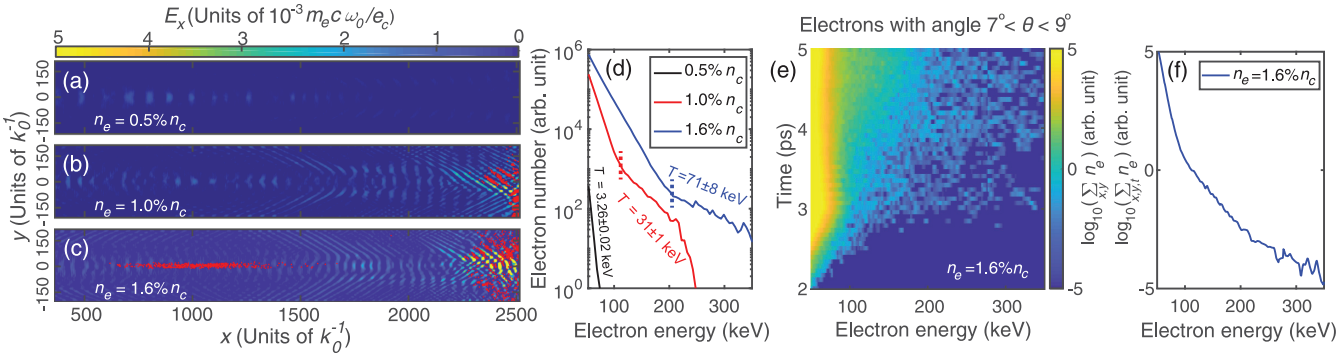

FIG. 3. (a)–(c) Electron plasma wave activity (laser propagating from left to right, entering at $x = 0$) for a peak laser intensity $I_0 = 1 \times 10^{17}$ Wcm^{-2} at $t = 4.3$ ps for electron densities: (a) $n_e = 0.5\%\ n_c$, (b) $n_e = 1.0\%\ n_c$, and (c) $n_e = 1.6\%\ n_c$, with electrons of energy $\varepsilon > 150$ keV overlaid as red circles. For clarity only 10% of these electrons are displayed in (c). (d) Net electron spectra of all electrons present in the simulation domain at $t = 4.3$ ps. The slope temperatures are given in (d) for the high energy portion of the spectra (minimum computed energy indicated by the dashed lines). (e) Histogram of electron density for the $n_e = 1.6\%\ n_c$ case, for all electrons accelerated at an angle equal to $8^\circ \pm 1^\circ$—similar to the collection angle of the electron spectrometer used experimentally. (f) Summation of the electron density shown in (e) for the whole simulated time.

simulations were performed, with longitudinal and transverse axes twice as large. Similar results including the position of high energy electron generation were exhibited, confirming there are negligible boundary effects. In all cases the field amplitude at the simulation boundaries is within the noise level. In Fig. 3(c), the electrons appear bunched together in the potential energy minima of the plasma waves, indicative of the SRS process in our parameter regime. For both the forward and near-forward SRS driven EPWs, the amplitude of E_x increases with increasing n_e. E_x reaches a maximum value of $E_x \sim 90$ GVm^{-1} in the high density case shown in Fig. 3(c) for the oblique EPWs, with the direct forward EPWs reaching only a fraction of this value. Note that electrons driven by the oblique EPWs will accelerate some electrons at angles approaching the laser axis (i.e., 0°), due to the crossing wave potential deflecting them from their original trajectory. This is visualized in Fig. 3(e), which displays a histogram of electron number density for the high density case for electrons accelerated with an angle of $8^\circ \pm 1^\circ$ which is comparable to the 7° viewing angle of the electron spectrometer as fielded in the experiment. Figure 3(f) displays a summation of electron density at these angles over the entire time of the simulation. The maximum electron energy in this angular band is similar to $\varepsilon_{\max}$ of the spectra shown in Fig. 2(a), indicating that the experimental observations are consistent with simulations that point to the presence of obliquely propagating EPWs.

For the high electron density case, we show in Fig. 4 the k spectrum of the E_x field. The near-forward SRS EPWs are evident in peaks at $(k_x, k_y) \sim (0.25, 0.36)$ and $(0.20, 0.28)$, both giving angles of ~55°. Since the laser is polarized in the plane, signals at $|k| \sim 1$ and 2 are also evident due to the laser propagating at nonzero angles, and to ion acoustic waves from stimulated Brillouin scattering [5,9] (a signal at $2k_0$ is also seen in the ion density) and electron density modulations at the second harmonic of the laser. The signal at $k_x = 0.13$ is evidence of direct forward SRS, and the signal at k_x in the range of 1.5–1.7 is a result of backward SRS. Although backscatter is not directly discussed here, we note that it initially grows prior to forward SRS in all the simulations but, for the plasma densities and temperatures examined, $k\lambda_d > 0.7$ for the resulting plasma waves. Therefore, SRS backscatter is subject to very strong damping and many nonlinear effects that saturate it at very low levels. Once forward SRS is dominant, the SRS backscatter does not grow similarly again, and therefore backscatter here does not exhibit burstiness like what has been observed, for example, in shock ignition relevant simulations and experiments of SRS [39,40]. Nonlinear effects such as the nonlinear frequency shift do not appear to be a factor in saturating forward SRS, nor are there any ion wave features indicative of saturation via the Langmuir decay instability. We also note here that we have performed other simulations with plane waves for similar parameters, and the angles observed for near-forward SRS are similar to the angles shown in Fig. 4. Simulations with a finite-width laser pulse but longer rise time (300 fs vs 50 fs) also show the same angle for near-forward SRS, though they show somewhat lower levels of direct forward scatter. In addition, simulations with a linear density variation $\Delta n_e = 0.1 n_e$ over the simulation domain also showed similar

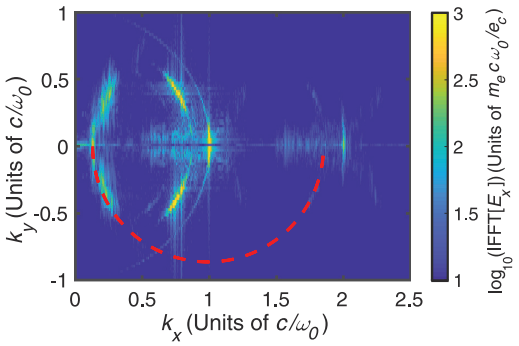

FIG. 4. Wave number spectrum of the longitudinal electric field (E_x) for peak laser intensity $I_0 = 1 \times 10^{17}$ Wcm^{-2} and electron density $n_e = 1.6\%\ n_c$ at time $t = 2.4$ ps, showing the angular dependence of the near-forward SRS and the spectrum present for other laser plasma instabilities. The red semicircle shows wave numbers in the lower half plane for which an electron plasma wave would satisfy k-matching conditions with an incident and scattered light wave.

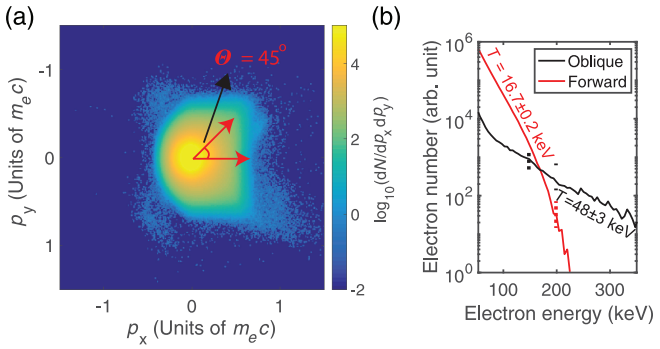

FIG. 5. (a) Electron phase space plot for a peak laser intensity $I_0 = 1 \times 10^{17}$ Wcm^{-2} and electron density $n_e = 1.6\%\ n_c$ at time $t = 4.3$ ps, showing the angular dependence of the accelerated electrons. The plasma wave angle (θ) is shown for the oblique wave. (b) Separate electron spectra (at $t = 4.3$ ps) showing those electrons accelerated due to forward SRS and those accelerated by near-forward SRS. Slope temperatures (T) are given; in the case of forward SRS-driven electrons the dashed red line indicates the cutoff energy the fit is performed to. In the case of oblique electrons, the dashed black line indicates the starting energy in the fit protocol.

results, and simulations with the laser polarized out of the simulation plane also showed near-forward SRS dominate at the right edge of the box. A more complete exploration of the complex interplay of multiple SRS processes and their saturation mechanisms for this parameter regime is left for future work.

We next consider how the forward and near-forward SRS processes contribute to the resultant electron spectra. Figure 5(a) displays the electron phase space for the high density case ($n_e = 1.6\%\ n_c$), clearly showing a peak in electron energy at an oblique angle with respect to the laser propagation direction. Figure 5(b) displays a snapshot of the electron spectra for electrons generated by near-forward and forward SRS at $t = 4.3$ ps. These two populations are discriminated by their location at $t = 4.3$ ps; electron energy spectra are plotted for electrons present at $x > 1500k_0^{-1}$ (labeled "Oblique") and $x < 1500k_0^{-1}$ (labeled "Forward"). These electron populations are accelerated predominantly by the EPWs located at those respective locations. From Fig. 5(b), it is clear that the vast majority of high energy electrons in the simulations are driven by the oblique EPWs. Quantitatively, this can be understood by considering that the oblique EPWs have a higher field amplitude, as seen in Figs. 3(b) and 3(c), and also that they have a lower measured (from simulations) phase velocity $v_\phi = \omega/k = 0.44c$ (where ω and k are the plasma wave frequency and wave number, respectively) than those generated by forward SRS ($v_\phi \sim c$). The trapping potential $U = |E|e_c/k \sim 50$ keV (where e_c is the electron charge) of the oblique EPW is close to $1/2 m_e v_\phi^2$ of the electron distribution (where m_e is the electron mass), meaning there is potential for a large number of electrons to be trapped in the oblique EPW and strong Landau damping [41] to occur, leading to acceleration of the trapped electrons. Compared to the slope temperature of the electrons in the region where the oblique EPW is driven ($x > 1500k_0^{-1}$) in Fig. 5(b), which is $T = 48 \pm 3$ keV, this further suggests that these hot electrons are generated by the oblique EPW driven by near-forward SRS.

With comparison to the experimental results, the slope temperature of the high temperature component exhibited experimentally, as shown in Fig. 2(a), is comparable to the oblique temperature in the simulations. Coupled with the similar cutoff energy in both simulations and experiment, we therefore attribute the high energy electrons measured experimentally to be accelerated by oblique EPWs. In the following section, we discuss via analytical methods the generation of EPWs driven by a propagating plane wave. We focus on the dependence of the near-forward SRS-driven EPW process on laser and target parameters, and the angular dependence of the resultant EPW responsible for electron acceleration.

IV. THEORY OF NEAR-FORWARD STIMULATED RAMAN SCATTERING AS A FUNCTION OF SCATTERING ANGLE, LASER INTENSITY, AND PLASMA DENSITY

The PIC simulations have shown that the spectrum of SRS-generated EPWs is congregated into a small range of angles and that the SRS scattered light corresponding to these EPWs is at an angle in the forward direction. As noted above, a similar observation was reported based on PIC simulations [27,28] for similar normalized laser amplitudes, slightly higher densities, and slightly higher temperatures. In these earlier publications, a geometrical picture was given for the existence of a critical angle for the EPW from SRS, which is also useful for the interpretation of the present work. It was shown from wave number matching that the magnitude of the EPW wave number (k) as a function of the incident laser wave number (k_0) and of the angle (θ) between k and k_0 is approximately given by

$$k = k_0 \cos\theta \pm \left(k_0^2 \cos^2\theta - 2k_p k_0\right)^{1/2}, \tag{1}$$

where $k_p \equiv \omega_p/c$. These values of k are shown in Fig. 4 as the dashed circle. This shows that the maximum θ is given by $\cos\theta_m = (2k_p/k_0)^{1/2}$, and from geometrical arguments this corresponds to a scattering angle of the light wave given by $\theta_{sm} = \pi/2 - \theta_m$. For angles of the EPW less than θ_m there are two solutions for θ_s and k which is why there is a $\pm$ in Eq. (1). As argued in Ref. [28], $d\theta/d\theta_s \approx 0$ near the maximum angle for θ_m, causing many modes to congregate near this angle.

The importance of this angle is further amplified due to arguments given by Wilks *et al.* [26]. They showed that when Landau damping is included, the spatial gain can be peaked at values of θ_s. For our parameters this also corresponds to values of θ near θ_m. This can be quickly seen by calculating $k\lambda_d$ at the critical angle. Using Eq. (1), it can be seen that $k\lambda_d \approx (2k_0/k_p)^{1/2} v_{th}/c$, where v_{th} is the electron thermal velocity. For the parameters of the experiment and the simulations, $k\lambda_d = 0.21$ at this angle. The magnitude of $dk/d\theta$ blows up at θ_m so that $k\lambda_d$ changes rapidly at this angle. Therefore, Landau damping could impact SRS with light scattering angles from π to $\pi/2 - \theta_m$.

To be more quantitative, we use linear spatial theory assuming the plasma wave can be described by fluid theory with a damping term. Under this assumption, the spatial growth

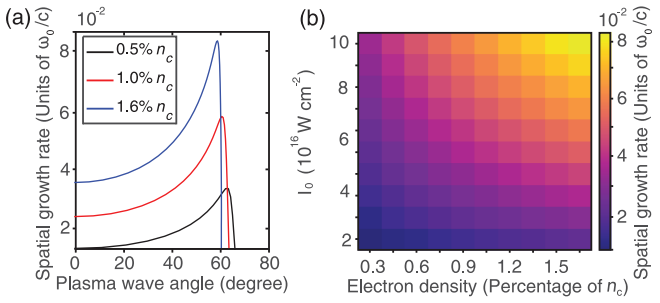

FIG. 6. (a) Spatial growth rate of the electron plasma wave (EPW) as a function of plasma wave angle for the three electron densities used in the simulations (0° refers to the angle of laser propagation) and peak laser intensity $I_0 = 10^{17}$ Wcm^{-2}. (b) Laser intensity and electron density map of the spatial growth rate of the EPW for the full domain investigated experimentally, at the angle of maximum growth rate for each case.

rate (κ) can be given by [26]

$$\kappa = \left[\frac{\gamma_0^2}{v_{gsx}v_{gpx}} + \frac{1}{4}\left(-\frac{\Gamma_p}{v_{gpx}}\right)^2\right]^{1/2} - \frac{\Gamma_p}{2v_{gpx}}, \tag{2}$$

where v_{gpx} and v_{gsx} are the x components of the group velocities of the plasma waves and scattered light waves, respectively, γ_0 is the maximum growth rate of SRS in a homogeneous plasma in the absence of any damping effects,

$$\gamma_0 = \frac{ka_0}{4}\left(\frac{\omega_p^2}{\omega(\omega_0-\omega)}\right)^{1/2}, \tag{3}$$

and Γ_p represents the Landau damping rate, given by

$$\Gamma_p = \left(\frac{\pi}{8}\right)^{1/2}\frac{\omega_p}{(k\lambda_d)^3}\exp[-(2k\lambda_d)^{-2} - 3/2]. \tag{4}$$

In Eqs. (2) and (3), $a_0 = e_c E_0/m_e\omega_0$ is the normalized vector potential or electron quiver velocity (where E_0 is the laser electric field amplitude) and $\lambda_d = \sqrt{\varepsilon_0 k_B T_e/e_c^2 n_e}$ is the Debye length. As a_0 and ω_p are intrinsically linked to I_0 and n_e, respectively, it is apparent that increasing either of these two terms results in a higher spatial growth rate. This formalism ignores the damping effects of electron-ion collisions, as the collision frequency (τ_c) is negligible for even the highest density case investigated here ($\tau_c \sim 70$ ps). The angular dependence varies according to the direction of propagation of the plasma waves and comes in via v_{gpx} and v_{gsx} which are given by

$$v_{gpx} = 3(k_0 - k_s\cos\theta_s)\left(v_e^2/\omega_p\right) = 3k\cos\theta v_{th}^2/\omega_p \tag{5}$$

for the plasma wave (where k_s is the scattered light wave number) and

$$v_{gsx} = k_s c^2\cos\theta_s/\omega_s \tag{6}$$

for the scattered light wave. Inserting the above formulas into Eq. (2) provides the spatial gain as either a function of θ_s or θ. In Fig. 6(a) we plot κ as a function of θ for the three electron densities and laser intensity ($I_0 = 10^{17}$ Wcm^{-2}) simulated. This clearly shows that the geometrical effects and the fact that Landau damping begins to affect EPWs for angles near θ_m leads to a pronounced peak in the spatial gain for angles near θ_m. We note that for the parameters considered in this paper, $k\lambda_d$ for large values of θ_s can even exceed unity. Therefore, the use of the fluid description with a Landau damping term will not work for these angles. However, this does not affect the range of angles plotted in Fig. 6. Figure 6(b) displays a matrix illustrating how κ changes with both n_e and I_0 at the optimum θ for EPW generation, for the entire parameter space investigated in this paper. κ strongly affects the level of SRS generated, and therefore the potential of the EPW, scaling exponentially. Therefore, a small drop in either laser intensity or electron density will significantly reduce the EPW field strength and result in less efficient electron acceleration, as seen both experimentally in Fig. 2 and in the simulations in Fig. 3. Qualitatively, Fig. 6 is in good agreement with these results, showing a strong peak κ for higher values of I_0 and n_e.

The optimum θ observed in the PIC simulations is close to this theoretical estimate. However, the theory assumes a plane wave pump while the simulations use a finite width laser. For such cases scattered light can leave the laser spot before it acquires the full spatial gain. Therefore, light scattering at larger angles (and the EPW for this scattered light angle) may not be amplified as much, leading to the largest growth occurring at smaller angles than that predicted in Fig. 6. We have, however, performed simulations with a plane wave and seen the largest EPWs are at similar angles.

In the simulations, two EPWs are driven oblique to the laser axis, accelerating electrons at the same angle with respect to the laser propagation direction on either side of the laser axis. As realized experimentally, this behavior would be expected to result in the acceleration of electrons in a cone around the laser axis bound by $\sim\theta$. As mentioned in Sec. III, this is due to the crossing wave structure of the oblique EPWs, resulting in a change of direction of a large portion of the accelerated electrons from the angle the oblique EPWs are driven. In reality the acceleration of electrons in such plasma waves can be rather complicated and perhaps even stochastic. The acceleration of the electrons is further complicated by the fact that the laser itself can cause electrons to be accelerated forward due to the $\mathbf{v}\times\mathbf{B}$ force. Since these electrons are also moving transversely due to the laser field they move obliquely forward. This was discussed in Ref. [27] and is seen in one-dimensional simulations of the experimental parameters. However, we have carried out simulations with the laser polarized out of the plane and still observe electrons moving forward at similar angles in the simulation plane.

V. CONCLUSIONS

This article reports on experimental and simulation results systematically exploring electron acceleration driven by near-forward SRS in the interaction of intense laser pulses with underdense helium plasma targets. For the higher density and laser intensity cases examined both in experiment and simulations, the electron spectrum in the near-forward direction fundamentally changed into a two-temperature distribution with $T = 34 \pm 1$ keV in the experiment, more than 10 times that at the lowest intensity and density case with measurable signal. Particle-in-cell simulations show that the high temperature component of the distribution is driven by near-forward SRS, preferentially exciting electron plasma waves

at large angles ($\theta \geqslant 45^\circ$) with respect to the laser propagation axis. The existence of a preferential oblique angle for forward scatter in correspondence with simulation and experimental results is supported by theoretical arguments given in Refs. [26–28].

ACKNOWLEDGMENTS

The authors would like to thank L. Yin, B. J. Albright, A. G. Seaton, J. Li, and H. Wen for fruitful discussions. The authors acknowledge the expertise of the Jupiter laser facility, Lawrence Livermore National Laboratory (LLNL). The authors would also like to acknowledge the support of the Center for High Energy Density Physics, LLNL. This work is supported by the US Department of Energy (DOE), National Nuclear Security Administration under Grant No. DE-NA0003943, and the DOE Department of Fusion Sciences under Grant No. DE-SC0019010. This research used resources from the National Energy Research Scientific Computing Center (NERSC), which is a DOE Science User Facility operated under Contract No. DE-AC02-05CH11231. S.Z. is supported by an MAE fellowship. The FLASH code used in this work was developed in part by the DOE NNSA ASC- and DOE Office of Science ASCR-supported Flash Center for Computational Science through Field Work Proposal No. 57789 to Argonne National Laboratory, Subcontract No. 536203 with Los Alamos National Laboratory, and Subcontract B632670 with LLNL.

[1] J. Nuckolls *et al.*, Nature (London) **239**, 139 (1972).
[2] R. S. Craxton *et al.*, Phys. Plasmas **22**, 110501 (2015).
[3] D. S. Montgomery, Phys. Plasmas **23**, 055601 (2016).
[4] J. F. Drake *et al.*, Phys. Fluids **17**, 778 (1974).
[5] D. W. Forslund *et al.*, Phys. Fluids **18**, 1002 (1975).
[6] P. Kaw, G. Schmidt, and T. Wilcox, Phys. Fluids **16**, 1522 (1973).
[7] R. K. Kirkwood *et al.*, Phys. Rev. Lett. **76**, 2065 (1996).
[8] W. L. Kruer *et al.*, Phys. Fluids **23**, 1326 (1980).
[9] D. W. Forslund *et al.*, Phys. Fluids **18**, 1017 (1975).
[10] S. H. Glenzer *et al.*, Phys. Rev. Lett. **106**, 085004 (2011).
[11] Workshop on the Science of Fusion Ignition on NIF, Lawrence Livermore National Laboratory Report, LLNL-TR-570412 (2012). Op cit. V. Gocharov and O. A. Hurricane, Panel 3 Report: Implosion Hydrodynamics, LLNL-TR-562104 (2012).
[12] C. Joshi *et al.*, Nature (London) **311**, 525 (1984).
[13] C. Joshi *et al.*, Phys. Rev. Lett. **47**, 1285 (1981).
[14] T. Döppner *et al.*, Phys. Rev. Lett. **108**, 135006 (2012).
[15] M. J. Rosenberg *et al.*, Phys. Rev. Lett. **120**, 055001 (2018).
[16] M. J. Rosenberg *et al.*, Phys. Plasmas **27**, 042705 (2020).
[17] R. E. Turner *et al.*, Phys. Rev. Lett. **57**, 1725 (1986).
[18] S. H. Batha *et al.*, Phys. Rev. Lett. **66**, 2324 (1991).
[19] R. Betti *et al.*, Phys. Rev. Lett. **98**, 155001 (2007).
[20] S. Gus'kov *et al.*, Phys. Rev. Lett. **109**, 255004 (2012).
[21] X. Ribeyre *et al.*, Phys. Plasmas **20**, 062705 (2013).
[22] W. Theobald *et al.*, Phys. Plasmas **22**, 056310 (2015).
[23] R. Nora *et al.*, Phys. Rev. Lett. **114**, 045001 (2015).
[24] S. Zhang *et al.*, Phys. Plasmas **27**, 023111 (2020).
[25] L. Yin, B. J. Albright, K. J. Bowers, W. Daughton, and H. A. Rose, Phys. Rev. Lett. **99**, 265004 (2007).
[26] S. C. Wilks *et al.*, Phys. Fluids **9**, 2794 (1992).
[27] D. W. Forslund, J. M. Kindel, W. B. Mori, C. Joshi, and J. M. Dawson, Phys. Rev. Lett. **54**, 558 (1985).
[28] W. B. Mori *et al.*, in *Laser Interaction and Related Plasma Phenomena*, Vol. 7, edited by H. Hora and G. H. Miley (Springer, Boston, 1986), p. 767.
[29] L. Yin *et al.*, Phys. Plasmas **26**, 082708 (2019).
[30] H. Chen *et al.*, Rev. Sci. Instrum **79**, 10E533 (2008).
[31] T. Bonnet *et al.*, Rev. Sci. Instrum **84**, 103510 (2013).
[32] A. Flacco *et al.*, Computer code NEUTRINO V941+, Laboratoire d'Utilisation des Lasers Intenses, Palaiseau, France, 2020; https://github.com/NeutrinoToolkit/Neutrino.
[33] See Supplemental Material at http://link.aps.org/supplemental/10.1103/PhysRevE.103.033203 for the data and analysis associated with both the interferometer and radiation-hydrodynamic simulations for plasma density measurements. References cited exclusively in the Supplemental Material are Refs. [42–44].
[34] P. Tzeferacos *et al.*, Phys. Plasmas **24**, 041404 (2017).
[35] R. A. Fonseca *et al.*, Lect. Notes Comput. Sci. **2331**, 342 (2002).
[36] R. G. Hemker, Ph.D. dissertation, University of California Los Angeles (2000), arXiv:1503.0276.
[37] R. A. Fonseca *et al.*, Plasma Phys. Control. Fusion **50**, 124034 (2008).
[38] M. R. Siegrist, Opt. Commun. **16**, 402 (1976).
[39] O. Klimo *et al.*, Plasma Phys. Controlled Fusion **56**, 055010 (2014).
[40] G. Cristoforetti *et al.*, High Power Laser Sci. **7**, E51 (2019).
[41] L. D. Landau, J. Phys. **10**, 25 (1946).
[42] M. J.-E. Manuel *et al.*, Phys. Rev. Lett. **122**, 225001 (2019).
[43] R. S. Craxton and R. L. McCrory, J. Appl. Phys. **56**, 108 (1984).
[44] M. E. Max, J. Arons, and A. B. Langdon, Phys. Rev. Lett. **33**, 209 (1974).